



Long-lived Bell states in an array of optical clock qubits

Nathan Schine ^{1,3}, Aaron W. Young ^{1,3}, William J. Eckner ^{1,3}, Michael J. Martin ^{1,2} and Adam M. Kaufman ¹ ⊠

The generation of long-lived entanglement in optical atomic clocks is one of the main goals of quantum metrology. Arrays of neutral atoms, where Rydberg-based interactions may generate entanglement between individually controlled and resolved atoms, constitute a promising quantum platform to achieve this. Here we leverage the programmable state preparation afforded by optical tweezers and the efficient strong confinement of a three-dimensional optical lattice to prepare an ensemble of strontium-atom pairs in their motional ground state. We engineer global single-qubit gates on the optical clock transition and two-qubit entangling gates via adiabatic Rydberg dressing, enabling the generation of Bell states with a state-preparation-and-measurement-corrected fidelity of 92.8(2.0)%(87.1(1.6)% without state-preparation-and-measurement correction). For use in quantum metrology, it is furthermore critical that the resulting entanglement be long lived; we find that the coherence of the Bell state has a lifetime of 4.2(6) s via parity correlations and simultaneous comparisons between entangled and unentangled ensembles. Such long-lived Bell states can be useful for enhancing metrological stability and bandwidth. In the future, atomic rearrangement will enable the implementation of many-qubit gates and cluster state generation, as well as explorations of the transverse field Ising model.

s the essential resource in quantum science, quantum entanglement enables a broad set of applications in computing, cryptography, and materials science, to name a few. One powerful application arises in metrology, where greater sensitivity and higher-bandwidth sensors are afforded by the properties of entangled multiparticle quantum states¹⁻⁸. Combining such enhancements with state-of-the-art time and frequency metrology⁹⁻¹⁴—namely, optical atomic clocks—has been a defining goal in this field of quantum metrology; the construction of a quantum-enhanced optical clock has broad implications for geodesy^{15,16}, gravitational-wave detection¹⁷⁻¹⁹ and the search for physics beyond the standard model²⁰.

A variety of approaches exist for creating metrologically useful entanglement. In neutral-atom optical lattice clocks, a number of methods have been proposed using cavity quantum electrodynamics, Rydberg interactions, or collisional interactions^{21–26}—indeed, recently, spin-squeezed states on an optical clock transition have been generated using collective cavity quantum electrodynamics interactions²⁷. In trapped ions, proposals and implementations of entanglement on optically separated qubits rely on spin-spin interactions mediated by Coulombic crystal modes, allowing efficient entanglement generation and Greenberger-Horne-Zeilinger states with as many as 24-ion optical qubits28 or photonic quantum networking between spatially distributed single-ion clocks²⁹. Given the control and measurements possible in modern atomic clock architectures, these systems offer the possibility of merging quantum information concepts with precision measurement. Utilizing entangling gates and protocols from quantum information science broadens the set of realizable quantum states, enabling new protocols for quantum metrology, while quantum error-correcting codes have opened routes for enhanced quantum sensing in the presence of noise and imperfect quantum resources³⁰⁻³⁴. In the context of optical atomic clocks, a number of recent protocols have advanced this union as a route to quantum-enhanced measurements^{30,33,35}, and in a very recent demonstration, the variational optimization of phase sensitivity at optical frequencies was implemented on a 26-ion quantum processor³⁵.

This theoretical and experimental momentum emphasizes the promise of combining control with scalability, to produce large-scale, entangled clocks amenable to versatile control and measurement schemes^{31,36,37}. An outstanding challenge in this regard is to pair these capabilities with long-lived quantum coherence so that many-particle states can be fruitfully leveraged for quantum-enhanced measurements at long interrogation times. A promising candidate for realizing this synergy is the recently demonstrated tweezer clock, which not only supplies long-lived atomic coherence and high stability^{38–40} but also large atom number^{39–42}, high-fidelity Rydberg interactions^{43–46} and microscopic control to engineer precisely tailored quantum systems.

In our previous work, we demonstrated state-of-the-art relative stability and atomic coherence using a tweezer-array clock^{38,40}. Here we advance our atomic control of the clock transition to elevate it into a high-fidelity qubit. We then implement entangling gates between these qubits through Rydberg excitations out of the excited qubit state, which realizes controllable Ising-type interactions^{43–48}.

With these capabilities, we achieve high-fidelity long-lived entanglement in an ensemble of Bell state pairs (Fig. 1a)^{43,44,46,49-53}. We employ an adiabatically resonant coupling of the qubit excited state to a Rydberg state to implement a controlled phase gate between two atomic qubits, up to single-atom lightshifts⁵⁴. Setting the controlled phase of our gate to be $\pi/2$ yields a controlled- \sqrt{Z} gate and enables the production of the Bell state $|\psi\rangle=\frac{1}{\sqrt{2}}(|gg\rangle+\mathrm{i}\,|ee\rangle)$, which has metrological relevance because the superposition components have a large energy separation. As such, clocks based on

¹JILA, University of Colorado and National Institute of Standards and Technology, and Department of Physics, University of Colorado, Boulder, CO, USA. ²Los Alamos National Laboratory, Los Alamos, NM, USA. ³These authors contributed equally: Nathan Schine, Aaron W. Young. [™]e-mail: adam.kaufman@colorado.edu

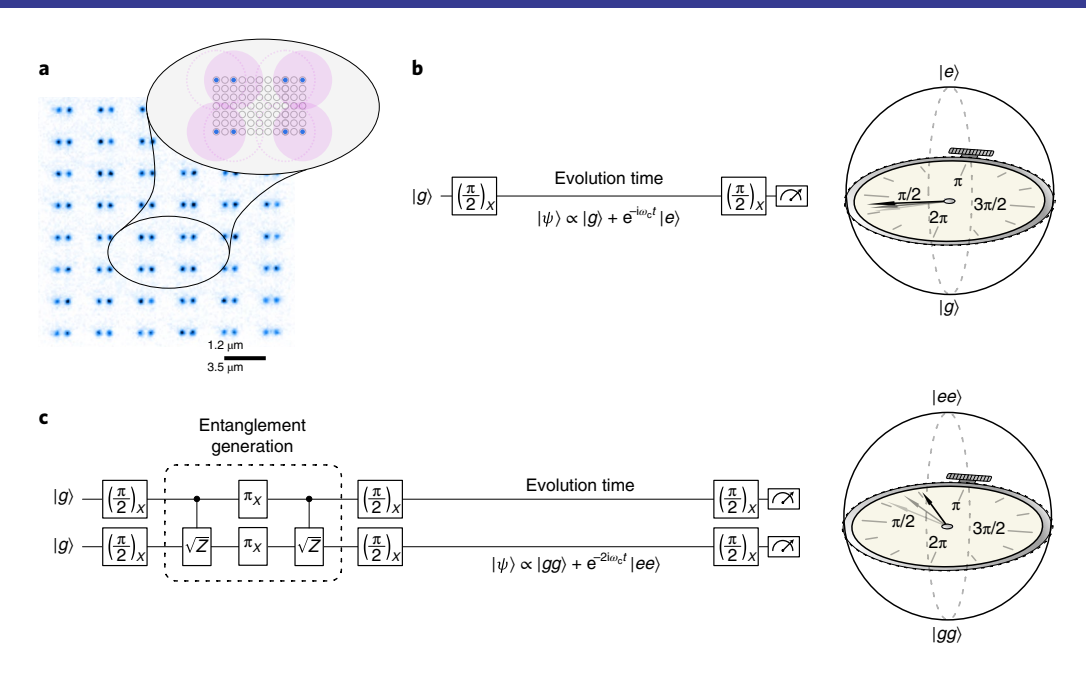


Fig. 1 | Quantum-enhanced optical frequency metrology. a, A tweezer array defines a 2D array of 1.2- μ m-separated doublets stochastically loaded and subsequently transferred into a 3D optical lattice (average image, blue). The inset shows that the two atoms within a doublet (blue, filled circles) are two lattice sites apart (grey, open circles), placing them well within the Rydberg blockade radius of each other (pink). The doublets are separated by six lattice sites (3.4 μ m) to preclude stray interactions between them. **b**, A standard clock measurement implements a Ramsey interferometer, in which each atom is prepared in an even superposition of the ground ($|g\rangle$) and clock ($|e\rangle$) states, namely, $|\psi\rangle = \frac{1}{\sqrt{2}}(|g\rangle + |e\rangle)$, and the clock interrogation proceeds by measuring the phase accrued by the atoms during the evolution time. On the Bloch sphere, this phase evolution corresponds to the Bloch vector precessing around the equator, acting like the hand on a stopwatch that revolves once every $\frac{2\pi}{oc} = 2.3$ fs, the inverse of the energy difference between $|g\rangle$ and $|e\rangle$; comparing the ticking of this stopwatch to a laser's oscillation is at the heart of an optical clock. **c**, With multiple atoms, additional laser pulses may prepare an entangled state, which is better for metrology. Here the Bell state $|\psi\rangle = \frac{1}{\sqrt{2}}(|gg\rangle + i|ee\rangle)$ is prepared by two controlled- \sqrt{Z} phase gates and global single-qubit gates. The phase between $|gg\rangle$ and $|ee\rangle$ evolves twice as fast during the evolution time, yielding a stopwatch that ticks twice as fast as that for a single atom. The faster ticking of such states holds the promise of higher-stability, higher-bandwidth optical clocks.

such states accrue phase more quickly than clocks based on unentangled atoms (Fig. 1b,c)3,55. We determine the fidelity with which we produce Bell states to be $\mathcal{F}=92.8(2.0)\%$ over a 6×8 array of atom pairs. To better understand near-term prospects for quantum metrological enhancement, we study the lifetime of these states in several ways. We observe the parity oscillation contrast and resulting fidelity to decay with a Gaussian 1/e time constant of $\sigma_F=407(13)$ ms³. However, the loss of atom–laser coherence can occur without the loss of atom–atom coherence, or in this case, relative coherence between distinct Bell states. Taking inspiration from the measurements of atomic coherence that reject the relative phase noise of the interrogation laser 11,40,56 , we measure Bell state parity and single-atom \hat{S}_z correlations to infer a 1/e exponential Bell state coherence time of $\tau_{bc}=4.2(6)$ s.

Our experiments begin with a tweezer-defined doublet array stochastically filled with $^{88}\mathrm{Sr}$ atoms (Fig. 1a). The atoms are implanted into a single plane of a co-located three-dimensional (3D) optical lattice, imaged, and subsequently cooled into their 3D motional ground state to achieve high-fidelity atomic control (Methods). We then apply a sequence of global laser pulses that drive the 1S_0 ($|g\rangle) \leftrightarrow ^3P_0$ ($|e\rangle$) clock transition resonantly with Rabi frequency Ω_c as well as the $|e\rangle \leftrightarrow |r\rangle$ Rydberg transition (to 5s40d $^3D_1; m_j = 0$) with Rabi frequency Ω_r and positive detuning Δ (Fig. 2a). Finally, we image the excited clock state atoms.

We implement a controlled phase gate for two clock-transition qubits using adiabatic Rydberg pulses, following the proposal of Mitra, et al. $^{54}.$ Each Rydberg pulse ramps $\varOmega_{\rm r}$ and \varDelta so that the clock state atoms adiabatically follow the instantaneous dressed clock-like eigenstate in the presence of the Rydberg coupling laser. This lightshifts the energy of a single clock state atom by

 $E_{\rm LS}^{(1)}=\frac{\hbar}{2}\left(-\Delta+\sqrt{\Omega_{\rm r}^2+\Delta^2}\right)$, where \hbar is the reduced Planck's constant. The energy shift of two non-interacting clock state atoms is $2E_{\rm LS}^{(1)}$. As shown in Fig. 2b, at close distances, such as two atoms within a single doublet, Rydberg blockade prevents the excitation of both atoms to the Rydberg state. The Hilbert space of two clock state atoms then reduces to an effective two-level system with states $|ee\rangle$ and $|b\rangle=\frac{1}{\sqrt{2}}(|er\rangle+|re\rangle)$ driven by a collectively enhanced Rabi frequency $\sqrt{2}\Omega_{\rm r}$ and detuning Δ . This lightshifts the energy of the $|ee\rangle$ state by $E_{\rm LS}^{(2)}=\frac{\hbar}{2}\left(-\Delta+\sqrt{2\Omega_{\rm r}^2+\Delta^2}\right)$. The difference $\kappa=E_{\rm LS}^{(2)}-2E_{\rm LS}^{(1)}$, is called the entangling energy, as it sets the energy scale of entangling operations 54 .

This adiabatic Rydberg pulse implements a controlled phase gate on the two-qubit states of a filled doublet, once the single-atom phase is removed. That is, the Rydberg pulse realizes the Hamiltonian

$$H_{\rm r} = E_{\rm LS}^{(1)} \hat{S}_z + \kappa |ee\rangle \langle ee|, \qquad (1)$$

where $\hat{S}_z = \mathbb{1} \otimes \hat{\sigma}_z/2 + \hat{\sigma}_z/2 \otimes \mathbb{1}$, $\hat{\sigma}_z$ is the Pauli z matrix and $\mathbb{1}$ is the identity matrix acting on the $(|e\rangle, |g\rangle)$ basis. We only consider single- and two-particle effects because the spacing between doublets is chosen to be large compared with the Rydberg interaction range (Fig. 1a). By implementing two of these Rydberg pulses separated by a π pulse, we remove the single-atom phase from \hat{S}_z ; therefore, the full sequence can be interpreted as containing two controlled phase gates, $U_c = |gg\rangle \langle gg| + |ge\rangle \langle ge| + |eg\rangle \langle eg| + e^i|ee\rangle \langle ee|$ with phase $\phi = -\int \kappa dt$ (Fig. 2c). Together, these three pulses implement Ising-type interactions $H_{\text{eff}} = \kappa \hat{S}_z^2$. We note that although fixed, large-detuning Rydberg dressing would produce equivalent coherent

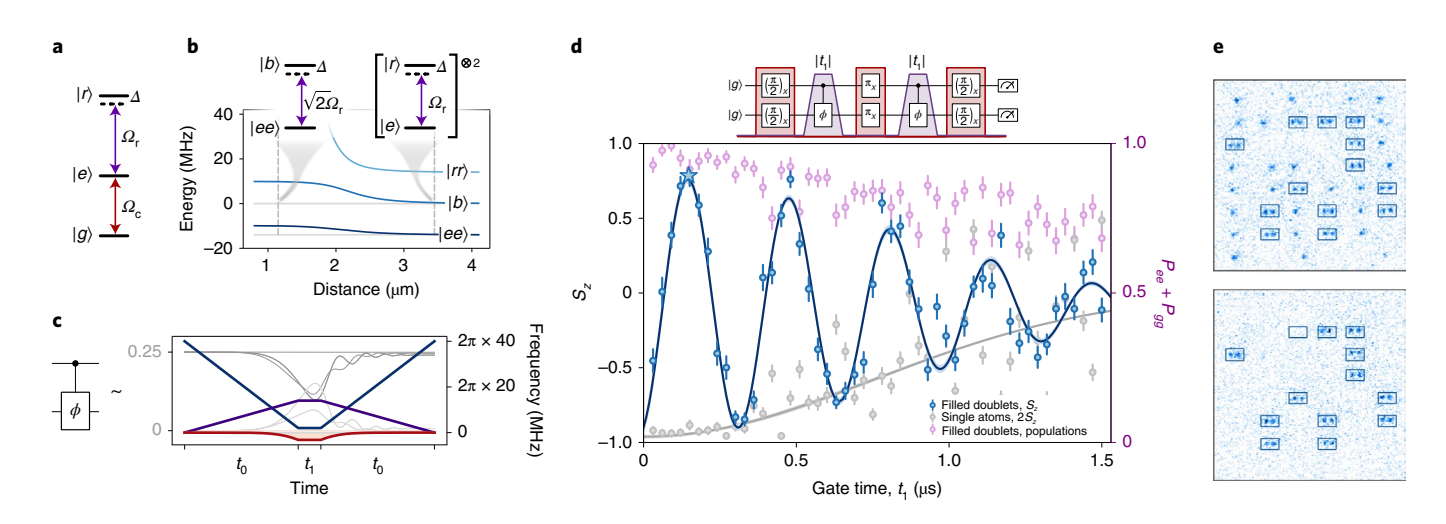


Fig. 2 | Clock-qubit-controlled phase gate via adiabatic Rydberg pulses. a, Ground ($|g\rangle$) and clock ($|e\rangle$) states define the clock transition qubit, which is resonantly driven with Rabi frequency Ω_c . We drive the clock state to a Rydberg state ($|r\rangle$) with controllable detuning Δ and Rabi frequency Ω_c . **b**, Considering the two-atom $|e\rangle - |r\rangle$ subsystem, at large distances (for example, interdoublet spacing, right vertical dashed line), the interactions between two Rydberg atoms are negligible. As the distance between atoms decreases (for example, intradoublet spacing, left vertical dashed line), Rydberg blockade causes an effective reduction in the Hilbert space to $|ee\rangle$ and $|b\rangle=\frac{1}{\sqrt{2}}(|er\rangle+|re\rangle)$. This modifies the lightshift on the $|ee\rangle$ state, providing the mechanism for entangling operations. **c**, By ramping both detuning (blue) and Rabi frequency (purple), we adiabatically follow the dressed $|ee\rangle$ state to small detuning to provide large entangling energy (red) and a fast controlled phase gate. A master equation model (Supplementary Information) tracks populations (left axis) within (dark grey) and outside (light grey) the two-qubit computational states as the gate progresses. The Rydberg state is populated only during the middle of the gate, d. To remove the effects of the large single-atom lightshift and provide the dynamics of only controlled phase gates, we implement a spin-echo gate sequence (top; timing not to scale): two adiabatic Rydberg pulses (purple trapezoids, to indicate adiabatic ramps of Rabi frequency and detuning) separated by a clock π pulse (red rectangles) implement an effective \hat{S}_{τ}^{2} Hamiltonian, and two surrounding clock $\pi/2$ pulses convert the resulting phase shifts into population oscillations between $|gq\rangle$ and $|ee\rangle$ (plotted as $S_z \equiv \langle \hat{S}_z \rangle$; blue, left axis) and nowhere else (pink, right axis). Meanwhile, non-interacting atoms (half-filled doublets; grey, left axis, plotted as $2\langle \hat{S}_z \rangle$ to match the vertical scales) undergo a 2π pulse and return to the ground state. For longer pulses, the spin-echo sequence fails to cancel the large single-atom lightshift, resulting in relaxation towards $S_{r}=0$ and population leaving the $|qq\rangle$ - $|ee\rangle$ subspace. All the error bars are the standard error of the mean (s.e.m.) from averaging over the array and 30 repetitions of the experiment, and the fit error bands represent 1σ uncertainty. e, We display an illustrative pair of images corresponding to the first peak of the interaction oscillation (star in d). The first image enables the identification of empty, half-filled and fully filled doublets, whereas the second image identifies clock state atoms after the gate sequence.

dynamics, adiabatically following the instantaneous eigenstates to resonance increases the ratio of interactions to dissipation, improving the gate fidelity (Supplementary Information).

We reveal the dynamics of the controlled phase gates by including them inside a Ramsey interferometry sequence (Fig. 2d, top), where the gate appears between two $\pi/2$ pulses. The first pulse establishes a superposition with a well-defined phase between $|g\rangle$ and $|e\rangle$ for each atom. The spin-echoed Rydberg pulses introduce an additional phase ϕ for the $|ee\rangle$ and $|gg\rangle$ components, and the final $\pi/2$ pulse closes the interferometer, converting those phases into an oscillation between $|gg\rangle$ and $|ee\rangle$ and removing the population from $|ge\rangle$ and $|eg\rangle$. The two $\pi/2$ pulses convert the effective Ising interactions of the middle three pulses into an S_r^2 interaction, which rotates $|gg\rangle$ into $|ee\rangle$. As shown in Fig. 2d, for short gate times, we observe these dynamics via $S_z \equiv \langle \hat{S}_z \rangle$ and $(P_{gg} + P_{ee})$ population measurements in filled doublets. For longer gate times, we observe that the failure of the spin echo causes a decay of S_z oscillations, as revealed in the dynamics of the single-atom S_z relaxing to zero. Furthermore, this causes the population to leave the $|gg\rangle - |ee\rangle$ subspace.

A zero crossing of S_z corresponds to the application of controlled phase gates of $\phi = \pi/2$ in under a microsecond, and after the full pulse sequence (Fig. 2d), the production of the Bell state $|\psi\rangle = \frac{1}{\sqrt{2}}(|gg\rangle + \mathrm{i}|ee\rangle)$. We benchmark our gates through fidelity \mathcal{F} , with which we create these Bell states, that is, $\mathcal{F} = \frac{1}{2} (P_{gg} + P_{ee} + C)$ (ref. 3). This depends on two factors: the sum of populations in the relevant states $(P_{gg} + P_{ee})$ as well as the coherence between them as accessed by contrast C in a parity oscillation measurement 3. At the first S_z zero crossing, we find $(P_{gg} + P_{ee}) = 0.955(28)$ or 0.922(27)

without state-preparation-and-measurement (SPAM) correction (Fig. 3a and Supplementary Information). To extract the Bell state coherence, we add a final 'analysis' $\pi/2$ pulse about a variable axis after completing the spin-echo sequence. In Fig. 3b, we plot the measured parity $\Pi \equiv \langle \hat{\Pi} \rangle = \langle \hat{\sigma}_z^l \hat{\sigma}_z^r \rangle$, where the superscript 'l' and 'r' denotes the left and right sites, respectively, within a doublet and the brackets imply averaging over the array and repetitions of the experiment. The amplitude of a sinusoidal fit versus the analysis phase yields the parity oscillation contrast C=0.919(28) and a resulting Bell-state fidelity of $\mathcal{F} = 92.8(2.0)\%$ (without SPAM correction, C = 0.838(19) and $\mathcal{F} = 87.1(1.6)\%$). The reported fidelity is reduced by 0.9(4)% to account for a systematic overestimation of P_{op} due to Rydberg state loss (Supplementary Information), and the uncertainty includes population and contrast uncertainty as well as uncertainty from SPAM correction, primarily from fluctuations of the imaging loss at the percent level.

The adiabatic Rydberg ramp speed and detuning endpoints are optimized to satisfy several competing constraints. Operating faster reduces the loss from the finite Rydberg-state lifetime (10.9(4) μs (Supplementary Information)), whereas operating slower results in greater adiabaticity so that atoms more completely return to the qubit states (Supplementary Information). We balance these competing effects with ramp durations of 250–350 ns (Methods). Master equation modelling (Fig. 2c and Supplementary Information) guided the experimental optimization of these parameters (Methods).

For metrological use, a long coherence time for the entangled state is desired. In Fig. 4, we investigate this timescale in several ways. First, we can simply wait before measuring the populations

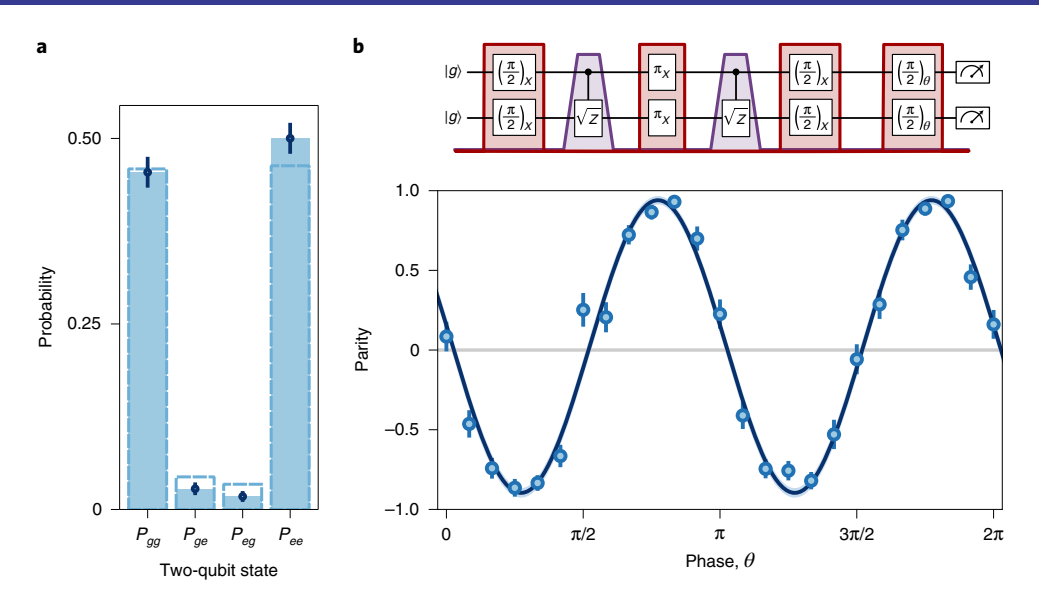


Fig. 3 | Bell-state fidelity. a, Array-averaged population fractions of two-qubit states reveal ($P_{gg} + P_{ee}$) = 0.955(28) (blue) after correcting for independently calibrated SPAM errors (3.5% total loss and infidelity). Uncorrected population measurements are shown by the dashed outlines. Ideal gate operation would yield $P_{gg} = P_{ee} = 0.5$. The error bars are the s.e.m. from averaging over the array and 100 repetitions of the experiment. **b**, We measure coherence C between |gg⟩ and |ee⟩ via the parity oscillation contrast. An analysis $\pi/2$ pulse about a variable axis is implemented by the composition of a single variable $\hat{\sigma}_z$ gate and a static $\pi/2$ pulse and produces two-particle states that oscillate in parity $\hat{\Pi} = \hat{\sigma}_z^i \hat{\sigma}_z^j$. The resulting data (blue points, SPAM corrected; error bars are s.e.m. from averaging over the array and 15 repetitions of the experiment) are fit by a sinusoid (blue curve; fit error band represents 1σ uncertainty). The amplitude of the sinusoidal fit yields C = 0.919(28). The uncertainty arises in approximately equal parts from the fit-parameter estimation uncertainty and systematic imaging loss fluctuations.

and parity oscillation contrast. Although the populations decay slowly (12.3(1.0) s exponential time constant for P_{ee} (Supplementary Information)), we find that the parity oscillation contrast decays rapidly, with a Gaussian 1/e time constant of $\sigma_{pc} = 407(13)$ ms (Fig. 4a). This loss of Bell-state-laser coherence could arise due to laser noise (in the rotating frame of the atoms), rather than atomic dephasing or decoherence effects. To investigate this possibility, we prepare the ensemble of single atoms in the array into a superposition state $(\frac{1}{\sqrt{2}}(|g\rangle - i|e\rangle))$ while preserving the Bell states' parity via an additional $\pi/2$ pulse about the $\varphi = 3\pi/4$ axis before the hold time. We find that the contrast of the array-averaged spin projection of single atoms, S2, decays with a longer exponential lifetime $\tau_{S_z} = 1.6(2)$ s. These measurements include a spin-echo clock π pulse halfway through the hold time to reject static and slow dephasing processes, which otherwise obscure the entanglement lifetime data in repetition- and array-averaged data (Methods). Separate measurements of the single-atom Ramsey contrast decay without a spin echo find an atom-laser coherence time consistent with τ_{S_z} .

At times beyond the coherence time with the laser, we investigate, in two ways, whether the Bell states retain coherence with respect to the rest of the array. First, we utilize parity–parity correlations, namely, $\langle (\hat{\Pi}_i - \bar{\Pi})(\hat{\Pi}_j - \bar{\Pi}) \rangle$, where $\bar{\Pi} = \langle \hat{\Pi}_i \rangle$ is the parity averaged over all the sites, repetitions, and analysis phases at a given hold time; $\langle \dots \rangle$ indicates an average over all the choices i and j of Bell states in a single shot of the experiment, followed by an average over all the repetitions and analysis phases. This quantity should decay at twice the rate of decay of the Bell state coherence, specifically the off-diagonal coherence of the two-particle density matrix defined in the frame of the other Bell states, and it is insensitive to the loss of atom–laser coherence (Supplementary Information). We find that the parity–parity correlation decays with an exponential time constant of $\tau_{III} = 2.3(4)$ s, indicating a Bell state coherence time of $\tau_{bc}^{III} = 4.6(7)$ s.

The parity-parity correlation decay effectively uses the relative phase within one Bell state as a reference against which to measure the coherence of another Bell state; by averaging over the array, this can be construed as comparing the evolving Bell-state phase with respect to the mean phase of all the other Bell states. However, rather than comparing Bell states with each other, we can also compare all of them with the ensemble of non-entangled atoms. More precisely, we compare the single-experiment average parity Π of the Bell states with the single-experiment average spin projection S_z of single atoms. However, because the Bell state parity oscillates twice as fast with the varying analysis phase as the single-atom S_z , we must first square the single-atom S_x to provide a reference signal that oscillates at the same frequency as the Bell-state parity (Fig. 4c-g). We construct the parity- S_z^2 correlation, $4\langle (\Pi - \bar{\Pi})(S_z^2 - \bar{S_z^2}) \rangle$, where (...) here indicates an average over all the repetitions and analysis phases, and $S_z^2 = \langle S_z^2 \rangle$. We find that this correlation decays with an exponential time constant of $\tau_{\Pi S_z^2} = 2.7(6)$ s. This decay is sensitive to both Bell state coherence decay and single-atom $S_z - \hat{S}_z$ correlation decay (Fig. 4b, grey; plotting $4\langle (\hat{S}_z^i - \bar{S}_z)(\hat{S}_z^j - \bar{S}_z) \rangle$), which has

lifetime $\tau_{S_zS_z} = 12.2(5)$ s; from these data, we infer a Bell state coherence time of $\tau_{\rm bc}^{IIS_z^2} = 3.4(1.1)$ s (Supplementary Information). Importantly, these correlations do not, by themselves, certify the presence of a Bell state, since there are non-entangled states that could

presence of a Bell state, since there are non-entangled states that could result in similar signals. However, Fig. 3 provides tomographic evidence for the initial generation of a Bell state, and these correlations then provide the Bell state coherence time with assumptions that certain exotic decay processes do not occur (Supplementary Information).

The comparison of the ensemble of Bell states to the ensemble of single atoms (Fig. 4c) is a simultaneous comparison between an entangled and unentangled pair of optical atomic clocks. The parametric plots of the entangled ensemble parity against the unentangled ensemble S_z and S_z^2 at hold times of less than a second form 2:1 and 1:1 Lissajous figures with zero relative phase, that is, a parabola and a line, respectively (Fig. 4d,e). The operation of a quantum-enhanced optical atomic clock requires the estimation

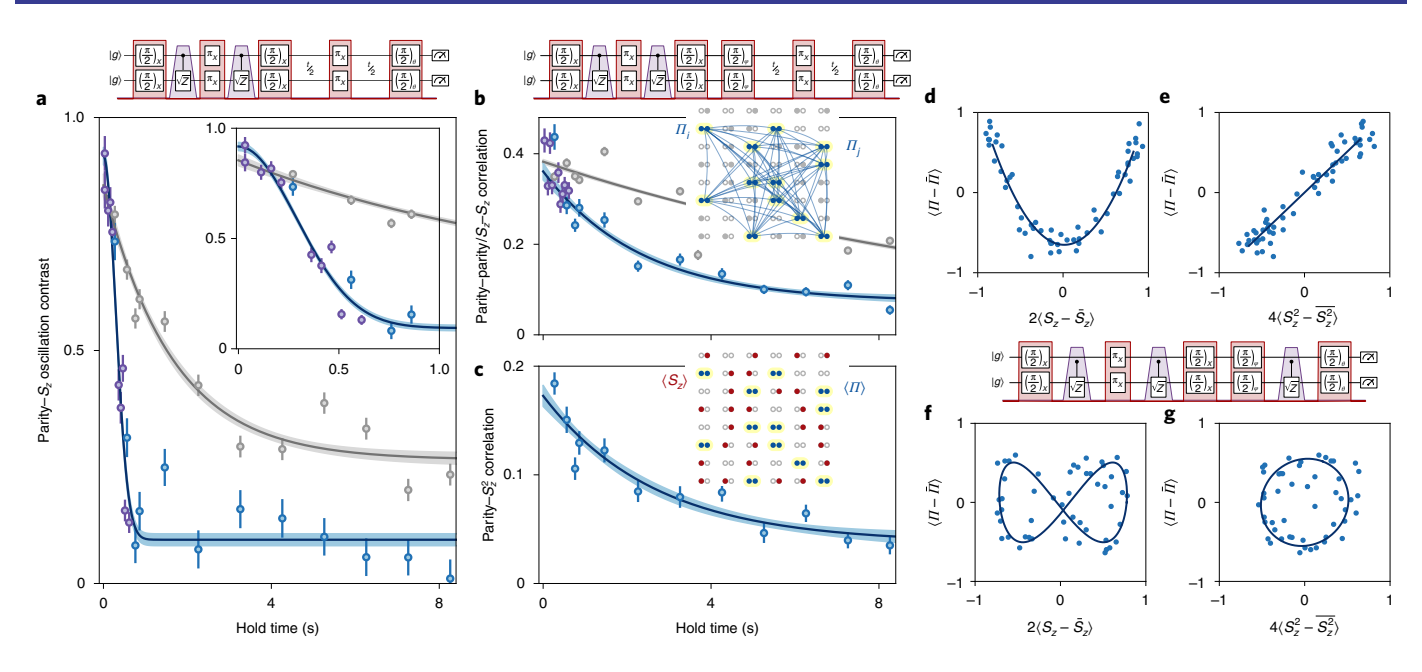


Fig. 4 | Bell-state coherence time. We estimate the Bell-states' coherence time through the decay of the parity oscillation contrast after a variable hold time (purple, first experimental schematic). We repeat this experiment and simultaneously prepare single atoms in a superposition state (via an additional $\pi/2$ pulse about an axis at $\omega = 3\pi/4$; second experimental schematic). **a.** The array-averaged single-atom spin oscillation contrast decays exponentially with a time constant $\tau_{S} = 1.6(2)$ s (dark grey), whereas the Bell states' parity oscillation contrast decays with a Gaussian with a 1/e time constant $\sigma_{\rm sc} = 407(13)$ ms (blue). The inset details short hold times and shares axes with the main panel. The error bars represent the 1σ confidence interval of the fitted sinusoidal amplitude. b, We access the Bell-state coherence time without dependence on atom-laser coherence via parity-parity correlations (main text). This decays with an exponential time constant of τ_{nn} = 2.3(4) s, providing a Bell state coherence time of $\tau_{bc}^{\Pi\Pi}$ = 4.6(7) s. For comparison, we measure the decay rate of the S_z - S_z correlation of single atoms (grey), τ_{S_z,S_z} = 12.2(5) s. **c**, An alternative handle on the Bell state coherence time comes from a comparison of the Bell state parity with the square of the single-atom array-averaged spin projection S_z . We find that this decays with an exponential time constant of $\tau_{IIS_z^2} = 2.7(6)$ s, from which we infer a Bell state coherence time of $\tau_{\rm bc}^{IIS_z^2} = 3.4(1.1)$ s. The error bars in **b** and **c** represent the s.e.m. from averaging the array-averaged correlation over repetitions and analysis phases. d,e, Parametric plots of the Bell state ensemble parity against the single-atom ensemble $S_{\epsilon}(\mathbf{d})$ and $S_{\epsilon}^{2}(\mathbf{e})$ at hold times of less than a second form 2:1 and 1:1 Lissajous figures with zero relative phase, that is, a parabola and a line, respectively. \mathbf{f}, \mathbf{g} , We introduce a relative phase difference between the entangled and unentangled ensembles with a third controlled- \sqrt{Z} pulse. This opens the 2:1 and 1:1 Lissajous figures into a figure of eight and ellipse, respectively, with a relative phase of $0.94(7)\frac{\pi}{3}$ radians. Panels **d-g** visually demonstrate the widely touted frequency doubling of Bell states' precession rate compared with single atoms, and squaring the single-atom signal matches the oscillation frequency. Note that the blue and grey data in a-e are derived from the same dataset, with 150 runs of the experiment per hold time. The fit error bands represent 1σ uncertainty.

of the relative phase difference between the reference and target clocks. To examine this, we inject a relative phase difference of $\pi/2$ with a third controlled- \sqrt{Z} pulse. This opens the 2:1 and 1:1 Lissajous figures into a figure of eight and ellipse, respectively, with a relative phase of $0.94(7.00)\frac{\pi}{2}$ radians measured via ellipse fitting (Fig. 4f,g). Future operation of this system in a quantum-enhanced simultaneous clock comparison may require establishing an optimal initial-phase difference and subsequently estimating the opening angle of the figure of eight or ellipse at an optimal interrogation time, whereas in situ comparison of an entangled and unentangled ensemble opens new routes for characterizing clock systematics and retaining enhanced metrological sensitivity in the presence of laser noise^{31,36,37}.

The two measurements of the Bell state coherence time from correlations are mutually consistent and may be combined to yield $\tau_{\rm bc} = 4.2(6)\,\rm s$. This, combined with our understanding of single-atom and laser decoherence mechanisms, provides an expected exponential decay time for the parity oscillation contrast of $0.69(10)\,\rm s$, longer than that shown in Fig. 4a. Nevertheless, the Bell state coherence time from correlations may be compared with an experimentally determined expectation given by half the single-atom atomic coherence time, that is, the decay rate of the S_z – S_z correlation of single atoms, namely, $\tau_{S_zS_z}=12.2(5)\,\rm s$. This value is understood in terms of single-atom population loss, decay and decoherence processes, up to an unexplained single-atom

lossless decoherence process with a four-minute timescale. This value is also consistent with the observed Bell state population dynamics, indicating the absence of correlated loss or decay processes (Supplementary Information). The nearly factor-of-three reduction in the Bell state coherence time from in situ correlation measurements could indicate the existence of an unidentified additional Bell state decoherence process with an approximately six-second timescale. However, the late-time behaviour of the correlations are consistent with single-atom measurements, and we hypothesize that the observed discrepancy is the result of technical noise that results in an additional, faster decoherence timescale at early times (Supplementary Information).

In this work, we have demonstrated the parallel generation of entangled Bell states on an optical clock transition using a novel spin-echoed adiabatically resonant Rydberg pulse sequence. We characterize the SPAM-corrected Bell-state fidelity to be $\mathcal{F}=92.8(2.0)\%$ and measure a 4.2(6) s array-averaged coherence time. These results establish a firm foundation for future explorations of quantum-enhanced optical frequency metrology at the stability frontier. A crucial near-term goal in this direction is to extend these results from pairs to clusters of several-to-tens of atoms, as well as to identify and generate the particular optimal quantum states of these clusters for a clock stability measurement quantum may further enhance the clock stability $^{33,58-60}$.

More broadly, we have demonstrated capabilities useful throughout quantum science. Although previous work has shown the control and detection of highly coherent qubits and scalability to large system sizes, here we have introduced maximally entangling gates, which enables a host of quantum applications. Particularly exciting goals include the generation of cluster states and with the addition of local measurements, subsequent demonstration of one-way quantum computing⁶¹. Explorations of the transverse-field Ising model with finite-range interactions are directly within reach. The combination of tweezer-based atom rearrangement and a 3D optical lattice further allows access to two-dimensional (2D) Hubbard physics with finite-range interactions.

Note added in proof: during preparation of this manuscript, we became aware of related work implementing a Mølmer–Sørensen gate with caesium atoms⁶².

Online content

Any methods, additional references, Nature Research reporting summaries, source data, extended data, supplementary information, acknowledgements, peer review information; details of author contributions and competing interests; and statements of data and code availability are available at https://doi.org/10.1038/s41567-022-01678-w.

Received: 20 December 2021; Accepted: 17 June 2022; Published online: 8 August 2022

References

- 1. Kitagawa, M. & Ueda, M. Squeezed spin states. Phys. Rev. A 47, 5138 (1993).
- Wineland, D. J., Bollinger, J. J., Itano, W. M. & Heinzen, D. Squeezed atomic states and projection noise in spectroscopy. *Phys. Rev. A* 50, 67 (1994).
- Sackett, C. A. et al. Experimental entanglement of four particles. Nature 404, 256–259 (2000).
- Esteve, J., Gross, C., Weller, A., Giovanazzi, S. & Oberthaler, M. Squeezing and entanglement in a Bose–Einstein condensate. *Nature* 455, 1216–1219 (2008).
- Burd, S. et al. Quantum amplification of mechanical oscillator motion. Science 364, 1163–1165 (2019).
- Tse, M. E. et al. Quantum-enhanced advanced LIGO detectors in the era of gravitational-wave astronomy. *Phys. Rev. Lett.* 123, 231107 (2019).
- Megidish, E., Broz, J., Greene, N. & Häffner, H. Improved test of local Lorentz invariance from a deterministic preparation of entangled states. *Phys. Rev. Lett.* 122, 123605 (2019).
- 8. Backes, K. et al. A quantum enhanced search for dark matter axions. *Nature* **590**, 238–242 (2021).
- Ushijima, I., Takamoto, M., Das, M., Ohkubo, T. & Katori, H. Cryogenic optical lattice clocks. Nat. Photon. 9, 185–189 (2015).
- McGrew, W. et al. Atomic clock performance enabling geodesy below the centimetre level. *Nature* 564, 87–90 (2018).
- 11. Marti, G. E. et al. Imaging optical frequencies with $100\,\mu\text{Hz}$ precision and $1.1\,\mu\text{m}$ resolution. *Phys. Rev. Lett.* **120**, 103201 (2018).
- Origlia, S. et al. Towards an optical clock for space: compact, high-performance optical lattice clock based on bosonic atoms. *Phys. Rev. A* 98, 053443 (2018).
- 13. Oelker, E. et al. Demonstration of 4.8×10⁻¹⁷ stability at 1 s for two independent optical clocks. *Nat. Photon.* 13, 714–719 (2019).
- 14. Brewer, S. M. et al. ²⁷Al⁺ quantum-logic clock with a systematic uncertainty below 10⁻¹⁸. Phys. Rev. Lett. 123, 033201 (2019).
- Mehlstäubler, T. E., Grosche, G., Lisdat, C., Schmidt, P. O. & Denker, H. Atomic clocks for geodesy. Rep. Prog. Phys. 81, 064401 (2018).
- Takamoto, M. et al. Test of general relativity by a pair of transportable optical lattice clocks. Nat. Photon. 14, 411–415 (2020).
- Kolkowitz, S. et al. Gravitational wave detection with optical lattice atomic clocks. Phys. Rev. D 94, 124043 (2016).
- Hu, L., Poli, N., Salvi, L. & Tino, G. M. Atom interferometry with the Sr optical clock transition. *Phys. Rev. Lett.* 119, 263601 (2017).
- 19. Abe, M. et al. Matter-wave atomic gradiometer interferometric sensor (MAGIS-100). *Quantum Sci. Technol.* **6**, 044003 (2021).
- Safronova, M. et al. Search for new physics with atoms and molecules. Rev. Mod. Phys. 90, 025008 (2018).
- Leroux, I. D., Schleier-Smith, M. H. & Vuletić, V. Implementation of cavity squeezing of a collective atomic spin. *Phys. Rev. Lett.* 104, 073602 (2010).
- Gil, L., Mukherjee, R., Bridge, E., Jones, M. & Pohl, T. Spin squeezing in a Rydberg lattice clock. *Phys. Rev. Lett.* 112, 103601 (2014).

 Strobel, H. et al. Fisher information and entanglement of non-Gaussian spin states. Science 345, 424–427 (2014).

- Zeiher, J. et al. Many-body interferometry of a Rydberg-dressed spin lattice. Nat. Phys. 12, 1095–1099 (2016).
- Cox, K. C., Greve, G. P., Weiner, J. M. & Thompson, J. K. Deterministic squeezed states with collective measurements and feedback. *Phys. Rev. Lett.* 116, 093602 (2016).
- Engelsen, N. J., Hosten, O., Krishnakumar, R. & Kasevich, M. A. Engineering spin-squeezed states for quantum-enhanced atom interferometry. In 2016 Conference on Lasers and Electro-Optics (CLEO) 1–2 (IEEE, 2016).
- Pedrozo-Peñafiel, E. et al. Entanglement on an optical atomic-clock transition. Nature 588, 414–418 (2020).
- Pogorelov, I. et al. Compact ion-trap quantum computing demonstrator. PRX Quantum 2, 020343 (2021).
- Nichol, B. et al. A quantum network of entangled optical atomic clocks. Preprint at https://arxiv.org/abs/2111.10336 (2021).
- 30. Tóth, G. & Apellaniz, I. Quantum metrology from a quantum information science perspective. *J. Phys. A: Math. Theor.* 47, 424006 (2014).
- Kessler, E. M., Lovchinsky, I., Sushkov, A. O. & Lukin, M. D. Quantum error correction for metrology. *Phys. Rev. Lett.* 112, 150802 (2014).
- Zhou, S., Zhang, M., Preskill, J. & Jiang, L. Achieving the Heisenberg limit in quantum metrology using quantum error correction. *Nat. Commun.* 9, 78 (2018).
- Kaubruegger, R., Vasilyev, D. V., Schulte, M., Hammerer, K. & Zoller, P. Quantum variational optimization of Ramsey interferometry and atomic clocks. *Phys. Rev. X* 11, 041045 (2021).
- Shettell, N., Munro, W. J., Markham, D. & Nemoto, K. Practical limits of error correction for quantum metrology. New J. Phys. 23, 043038 (2021).
- 35. Marciniak, C. D. et al. Optimal metrology with programmable quantum sensors. *Nature* **603**, 604–609 (2022).
- Borregaard, J. & Sørensen, A. S. Near-Heisenberg-limited atomic clocks in the presence of decoherence. *Phys. Rev. Lett.* 111, 090801 (2013).
- Pezzè, L. & Smerzi, A. Heisenberg-limited noisy atomic clock using a hybrid coherent and squeezed state protocol. *Phys. Rev. Lett.* 125, 210503 (2020).
- Norcia, M. A. et al. Seconds-scale coherence on an optical clock transition in a tweezer array. *Science* 366, 93–97 (2019).
- Madjarov, I. S. et al. An atomic-array optical clock with single-atom readout. Phys. Rev. X 9, 041052 (2019).
- Young, A. W. et al. Half-minute-scale atomic coherence and high relative stability in a tweezer clock. *Nature* 588, 408–413 (2020).
- Scholl, P. et al. Quantum simulation of 2D antiferromagnets with hundreds of Rydberg atoms. *Nature* 595, 233–238 (2021).
- 42. Ebadi, S. et al. Quantum phases of matter on a 256-atom programmable quantum simulator. *Nature* **595**, 227–232 (2021).
- Levine, H. et al. Parallel implementation of high-fidelity multiqubit gates with neutral atoms. *Phys. Rev. Lett.* 123, 170503 (2019).
- Graham, T. et al. Rydberg-mediated entanglement in a two-dimensional neutral atom qubit array. Phys. Rev. Lett. 123, 230501 (2019).
- 45. Madjarov, I. S. et al. High-fidelity entanglement and detection of alkaline-earth Rydberg atoms. *Nat. Phys.* **16**, 857–861 (2020).
- Ma, S. et al. Universal gate operations on nuclear spin qubits in an optical tweezer array of ¹⁷¹Yb atoms. *Phys. Rev. X* 12, 021028 (2022).
- Wilk, T. et al. Entanglement of two individual neutral atoms using Rydberg blockade. *Phys. Rev. Lett.* 104, 010502 (2010).
- Isenhower, L. et al. Demonstration of a neutral atom controlled-NOT quantum gate. Phys. Rev. Lett. 104, 010503 (2010).
- Leibfried, D. et al. Experimental demonstration of a robust, high-fidelity geometric two ion-qubit phase gate. *Nature* 422, 412–415 (2003).
- Kirchmair, G. et al. High-fidelity entanglement of ⁴³Ca⁺ hyperfine clock states. Phys. Rev. A 79, 020304 (2009).
- Ballance, C., Harty, T., Linke, N., Sepiol, M. & Lucas, D. High-fidelity quantum logic gates using trapped-ion hyperfine qubits. *Phys. Rev. Lett.* 117, 060504 (2016).
- Gaebler, J. P. et al. High-fidelity universal gate set for ⁹Be⁺ ion qubits. Phys. Rev. Lett. 117, 060505 (2016).
- Shapira, Y., Shaniv, R., Manovitz, T., Akerman, N. & Ozeri, R. Robust entanglement gates for trapped-ion qubits. *Phys. Rev. Lett.* 121, 180502 (2018).
- Mitra, A. et al. Robust M
 ølmer-Sørensen gate for neutral atoms using rapid adiabatic Rydberg dressing. Phys. Rev. A 101, 030301 (2020).
- Kessler, E. M. et al. Heisenberg-limited atom clocks based on entangled qubits. *Phys. Rev. Lett.* 112, 190403 (2014).
- Chou, C. W., Hume, D. B., Koelemeij, J. C. J., Wineland, D. J. & Rosenband, T. Frequency comparison of two high-accuracy Al⁺ optical clocks. *Phys. Rev. Lett.* 104, 070802 (2010).
- Khazali, M., Lau, H. W., Humeniuk, A. & Simon, C. Large energy superpositions via Rydberg dressing. *Phys. Rev. A* 94, 023408 (2016).
- Davis, E., Bentsen, G. & Schleier-Smith, M. Approaching the Heisenberg limit without single-particle detection. *Phys. Rev. Lett.* 116, 053601 (2016).

- Hosten, O., Krishnakumar, R., Engelsen, N. J. & Kasevich, M. A. Quantum phase magnification. *Science* 352, 1552–1555 (2016).
- Schulte, M., Martínez-Lahuerta, V. J., Scharnagl, M. S. & Hammerer, K. Ramsey interferometry with generalized one-axis twisting echoes. *Quantum* 4, 268 (2020).
- Briegel, H. J., Browne, D. E., Dür, W., Raussendorf, R. & Van den Nest, M. Measurement-based quantum computation. *Nat. Phys.* 5, 19–26 (2009).
- 62. Martin, M. J. et al. A Mølmer-Sørensen gate with Rydberg-dressed atoms. Preprint at https://arxiv.org/abs/2111.14677 (2021).

Publisher's note Springer Nature remains neutral with regard to jurisdictional claims in published maps and institutional affiliations.

This is a U.S. Government work and not under copyright protection in the US; foreign copyright protection may apply 2022

Methods

Apparatus. Loading, cooling and imaging of ⁸⁸Sr atoms is described elsewhere⁶³. The radio-frequency source for the generation of the 515 nm tweezer array is described elsewhere⁴⁰. We use a 3D clock-magic optical lattice at 813 nm as the primary science potential for imaging, clock rotations and Rydberg spectroscopy (Extended Data Fig. 1 and Supplementary Information). This potential enables efficient cooling and high-contrast clock rotations, as discussed below.

We open the ⁸⁸Sr ${}^{1}S_{0} \leftrightarrow {}^{3}P_{0}$ optical clock transition by applying a vertically oriented magnetic field with a magnitude of up to 550 G. This is accomplished using our main (magneto-optical trap) coils driven by a remotely controlled Delta Elektronika (SM30-200) supply. We drive the clock transition using approximately 13 mW of 698 nm laser light focused by a 150 mm cylindrical lens. The clock laser source is a series of three diodes injection locked to the light stabilized to a cryogenic silicon cavity¹³. The path from the reference laser to our experiment includes 60 m of fibre and approximately 2 m of free space, which are noise cancelled, with the reference mirror attached to the main objective mount. In addition, there is approximately 1 m of propagation that includes the second injection-locked diode which is not noise-canceled. Given the stability shown in our previous work with similar lengths of uncancelled free-space propagation⁴⁰, we do not expect the added phase noise from the uncancelled path length to limit the clock-pulse fidelity. As shown in Extended Data Fig. 2a, we can drive the clock transition with a Rabi frequency in excess of 1 kHz and with a π -pulse fidelity of 99.41(57)%. This represents a substantial increase over approximately 80% fidelity shown in our previous work40

Our high-fidelity clock rotations are enabled by the improved spatial confinement afforded by a deep, power-efficient 3D lattice as opposed to shallow tweezers. Tight confinement enables resolved sideband cooling after transfer into the lattice, yielding a reduced average phonon number $\bar{n}=0.04^{+0.11}_{-0.04}$ in the direction of clock laser propagation. Tight confinement also manifests as a high 99 kHz trap frequency and correspondingly small Lamb–Dicke parameter $\eta=0.22$. Both lower temperature and smaller Lamb–Dicke parameter result in the reduced motional dephasing of Rabi oscillations, yielding an expected (ideal) π -pulse fidelity of $99.98^{+0.02}_{-0.09}\%$. In typical experiments, however, we observe some heating that limits the clock π -pulse fidelity to a maximum of 99.79% (Supplementary Information), which may be compared with our observed clock π -pulse fidelity of 99.41(57.00)%.

We connect the clock state to a Rydberg state using an ultraviolet (UV) laser near 317 nm with approximately 1 W power. The UV laser system first produces 634 nm light via single-pass sum-frequency generation of 1,066 and 1,569 nm. A final stage of second-harmonic generation inside a resonant cavity converts 634 nm light into 317 nm light (Supplementary Information). We drive the transition from the clock state to the 5s40d 3D_1 (m_j =0) Rydberg state with Rabi frequencies up to Ω_r = $2\pi\times18$ MHz. We choose a D state rather than an S state due to its greater dipole matrix element, which directly increases the entangling energy in our adiabatically resonant pulse scheme, whereas the reduced van der Waals C_6 interaction coefficient is still sufficient to ensure blockade at the 1.1 μ m intradoublet separation and enabling denser doublet spacings. We observe Rydberg spectra and Rabi oscillations through the loss of clock-state atoms (Extended Data Fig. 2b). Perhaps surprisingly, the observed contrast is consistent with the 1/9 branching ratio of intermediate triplet S states back into the clock state versus all 5s5p 3P , states.

Experiments. Our experiments begin by preparing a magneto-optical trap, loading and cooling single atoms into a 515-nm-wavelength tweezer array, transferring those atoms into a single plane of a 3D optical lattice at 813 nm, imaging the location of those atoms and cooling the atoms, resulting in >90% of the atoms in their 3D motional ground state (Extended Data Fig. 3, state prep). This process has been largely described in our previous work***. except for the transfer into and cooling in the 3D optical lattice. The loss due to transfer from tweezers into well-aligned lattice sites is negligible; however, the global alignment of the tweezer array to the underlying lattice is not perfectly commensurate, resulting in 'slips' in the spacing of atoms in the lattice, which causes variable imaging performance. Furthermore, we find that the relative spatial phase between the tweezer array and lattice drifts by a lattice site over the course of several hours. Improving the alignment and stability of this system will be the subject of future work.

Ground-state cooling proceeds similarly to cooling in 813 nm tweezers described in previous work \$^{40,63}\$. Achieving a magic angle between the applied magnetic field and optical polarization enables efficient cooling to the 3D motional ground state. This does require, however, that the axial lattice be vertically polarized, which makes it less power efficient and leads to the formation of an out-of-phase horizontally polarized lattice, too. Nevertheless, we typically achieve 3D ground-state fractions above 90%, although the exact performance can vary on a day-to-day basis.

Having prepared an ensemble of ground state atoms in known positions in the lattice, we are ready to perform our experiments. To open the clock transition, we apply a large magnetic field. Although we can apply a field of up to $550\,\mathrm{G}$ to yield a clock Rabi frequency above $1\,\mathrm{kHz}$, we typically apply a $55\,\mathrm{G}$ field, resulting in a $100\,\mathrm{Hz}$

clock Rabi frequency. The use of lower fields slows the gate and does not substantially affect the gate fidelity, but it does reduce the magnetic-field noise, which otherwise limits parity-oscillation decay times to several tens of milliseconds due to the fluctuating quadratic Zeeman shift of the clock state (Supplementary Information).

Throughout the experimental sequence, we hold the axial lattice low at approximately $8E_p$, whereas we ramp the 2D lattice high to $420E_r$ for all the clock pulses, low to $12E_r$ for all the Rydberg pulses and $37E_r$ for all the hold times. Note that E_r refers to the recoil energy of a single 813 nm photon. Ramping the 2D lattice high provides strong confinement for a low Lamb–Dicke parameter (η =0.22), which enables high-fidelity clock pulses, whereas ramping the 2D lattice low reduces the total lattice-induced lightshift on the Rydberg line to ~200 kHz. This is sufficiently low such that lattice inhomogeneity does not affect gate fidelity, and leaving the lattice on provides atomic confinement. Experiments with the lattice switched off during the UV pulses can result in atomic heating, increased loss and lower gate fidelity.

We implement the adiabatic Rydberg-dressing gate scheme of Mitra, et al.⁵⁴ due to its reduced sensitivity to several sources of gate errors relative to the resonant gate scheme of Levine, et al.⁴³. In particular, we benefit from the robustness to blockade errors or Rydberg laser intensity (Rabi frequency) errors that populate the doubly excited Rydberg state^{54,64}. Moreover, the timing resolution of our experimental system would necessitate a reduction in the Rydberg Rabi frequency to implement the resonant gate scheme.

Finally, in the relevant experiments with a variable hold time, we perform a spin-echo clock π pulse to remove dephasing due to spatial inhomogeneity of the clock frequency. This inhomogeneity arises from the lattices that confine the atoms—since their optical frequencies are separated by 160 MHz, both lattices cannot simultaneously be at the clock-magic wavelength. Combined with the ~50% peak-to-peak inhomogeneity of the combined lattice depth across the atom array, this yields a lightshift inhomogeneity of ~0.1 Hz. This causes a significant reduction in the various correlation decay times measured in Fig. 4. By introducing a π pulse in the middle of the hold time, we greatly reduce the effects of inhomogeneity across the array, as evident in the spatially resolved parity–parity correlation measurements (Extended Data Fig. 4).

Data availability

The experimental data presented in this manuscript are available upon request and through Zenodo (https://doi.org/10.5281/zenodo.6626065).

References

- Norcia, M. A., Young, A. W. & Kaufman, A. M. Microscopic control and detection of ultracold strontium in optical-tweezer arrays. *Phys. Rev. X* 8, 041054 (2018).
- Jaksch, D. et al. Fast quantum gates for neutral atoms. Phys. Rev. Lett. 85, 2208 (2000).

Acknowledgements

We acknowledge J. Ye and his lab, particularly D. Kedar, for the operation and provision of the silicon-crystalline-cavity-stabilized clock laser and helpful conversations. We thank I. Deutsch, A. M. Rey, C. Sanner and A. Cao for fruitful discussions and feedback on the manuscript. A.M.K. acknowledges support from ARO grant no. W911NF-19-1-0223, AFOSR grant no. FA9550-19-1-0275, DOE Quantum System Accelerator (QSA) grant no. 7565477+, NSF QSEnSE QLCI-2016244, NSF JILA-PFC PHY 1734006 and NIST. N.S. acknowledges support from the NRC research associateship program. W.J.E. acknowledges support from the NDSEG. M.J.M. was supported by the Laboratory Directed Research and Development program of Los Alamos National Laboratory under project nos. 20190494ER and 20200015ER.

Author contributions

The experiment was designed and built by N.S., A.W.Y., W.J.E. and A.M.K. N.S., A.W.Y. and W.J.E. operated the experiment and analysed the data. All the authors contributed to the manuscript.

Competing interests

The authors declare no competing interests.

Additional information

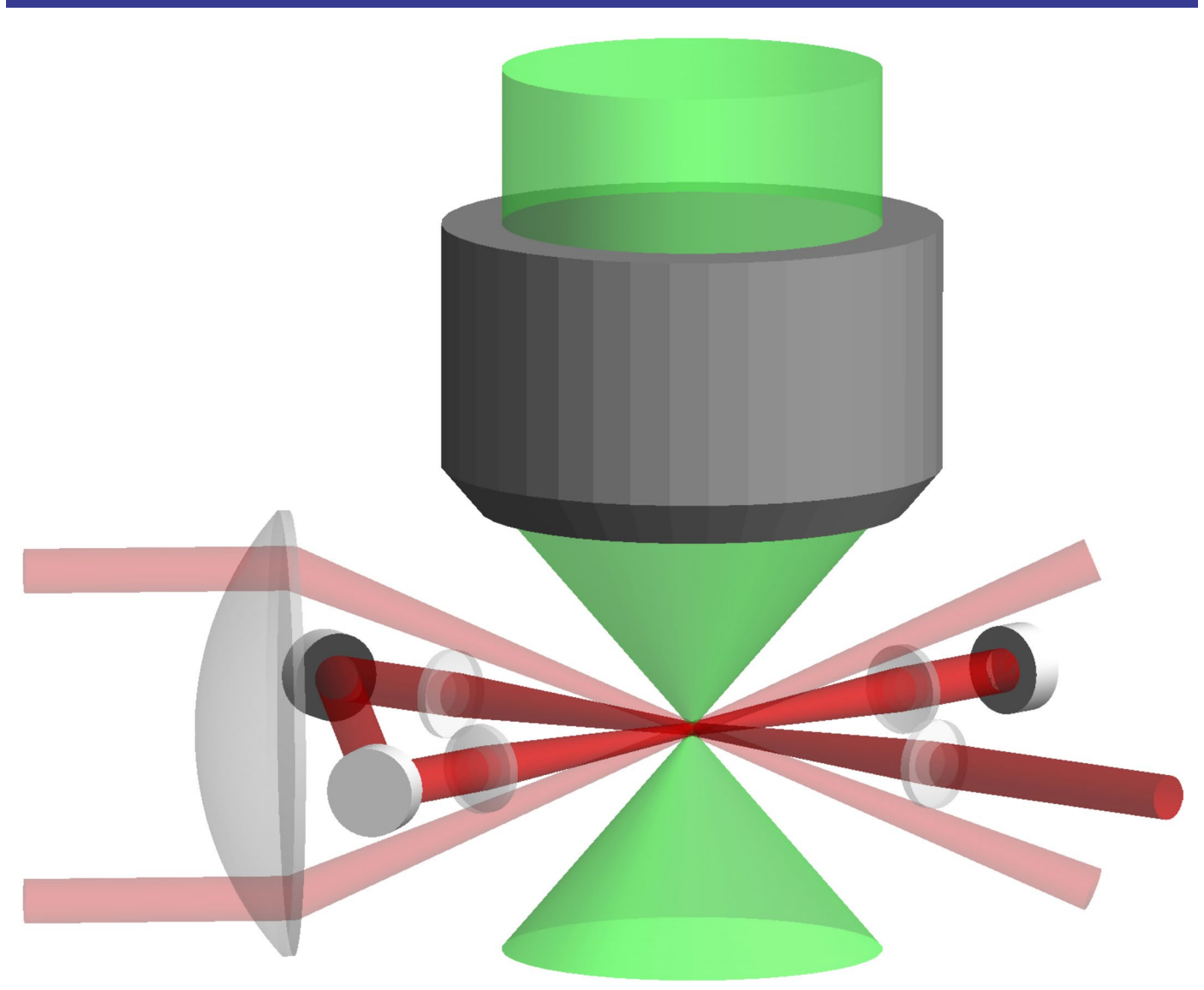
Extended data is available for this paper at https://doi.org/10.1038/s41567-022-01678-w.

 $\label{thm:contains} \textbf{Supplementary information} \ The online version contains supplementary material available at $$https://doi.org/10.1038/s41567-022-01678-w.$

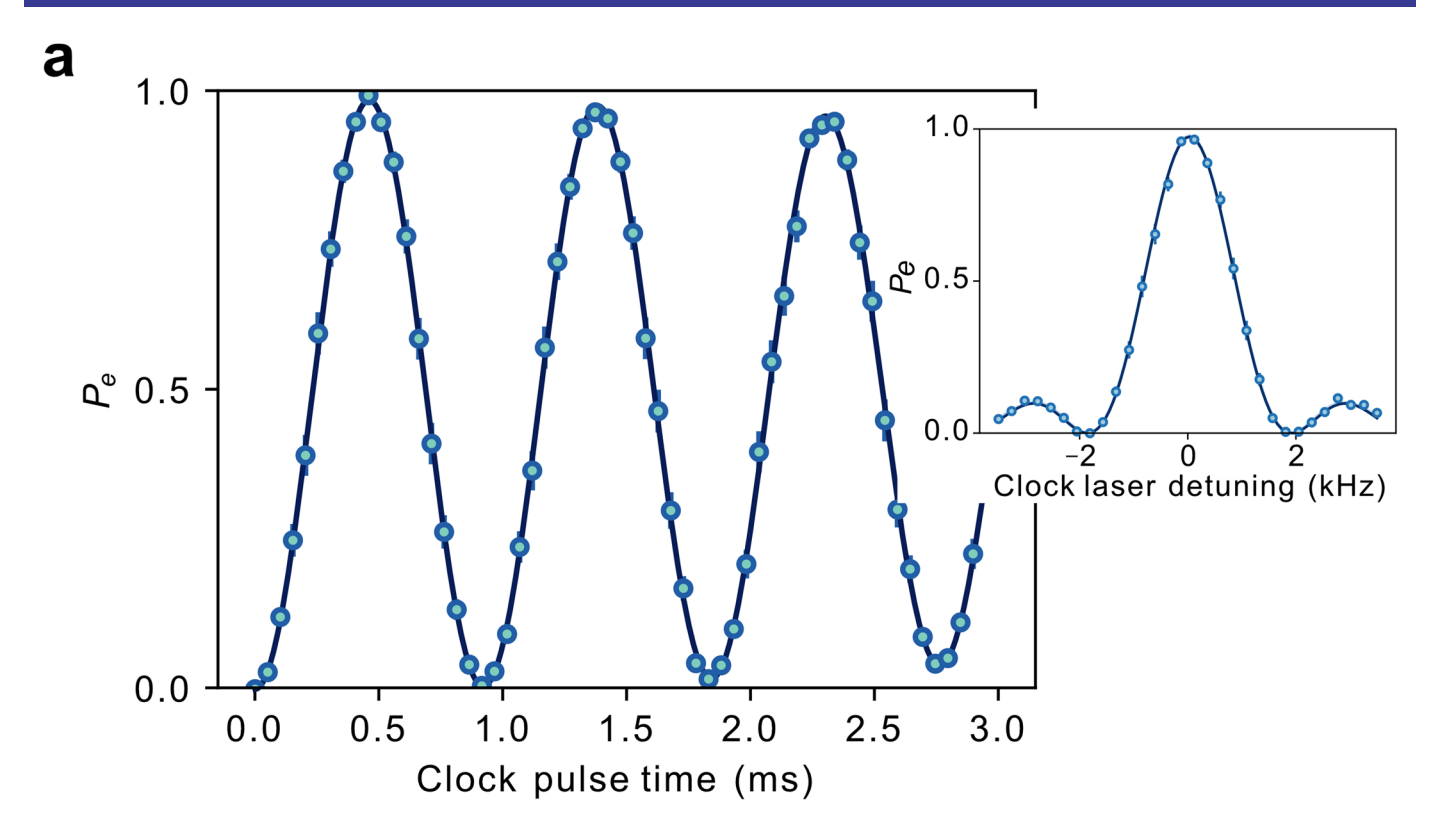
Correspondence and requests for materials should be addressed to Adam M. Kaufman.

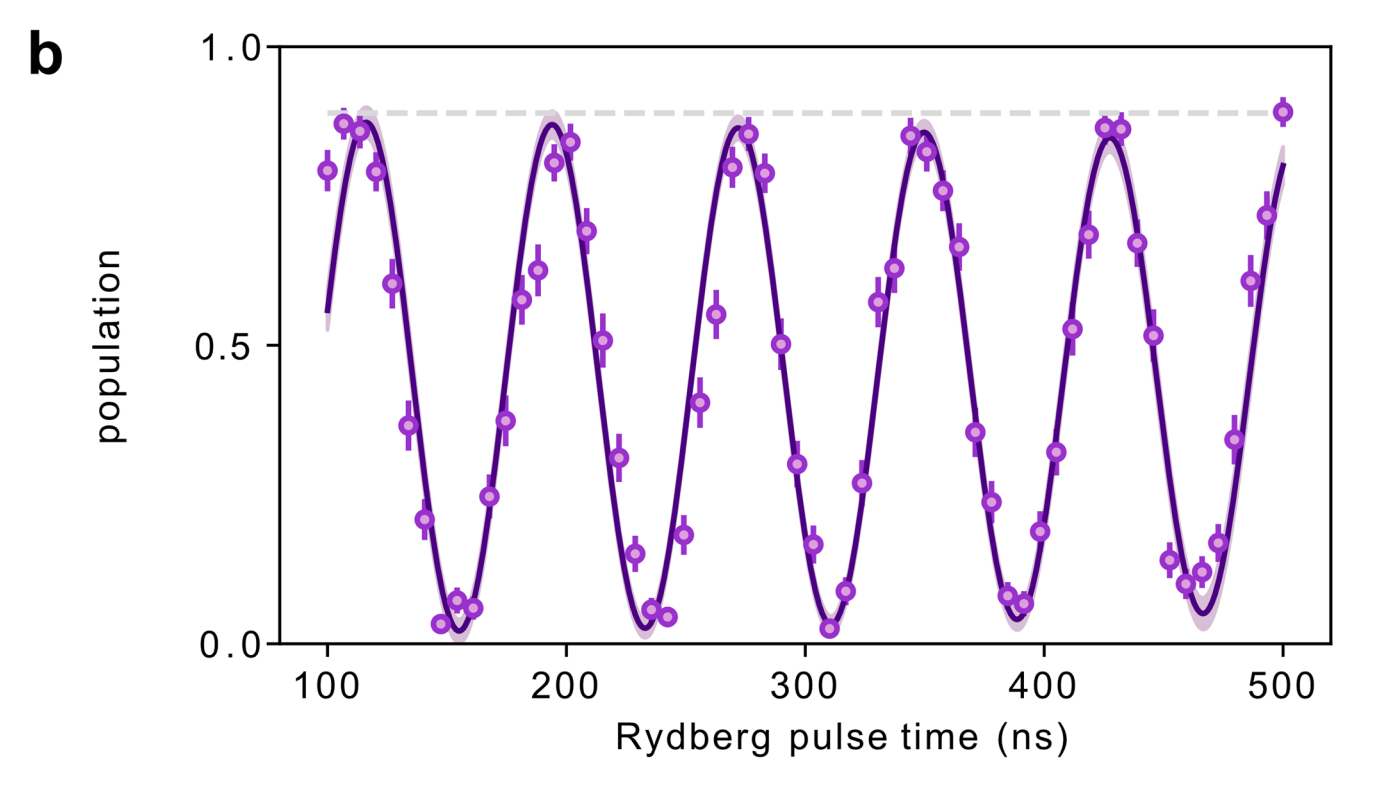
Peer review information *Nature Physics* thanks Jacob Covey and the other, anonymous, reviewer(s) for their contribution to the peer review of this work.

Reprints and permissions information is available at www.nature.com/reprints.

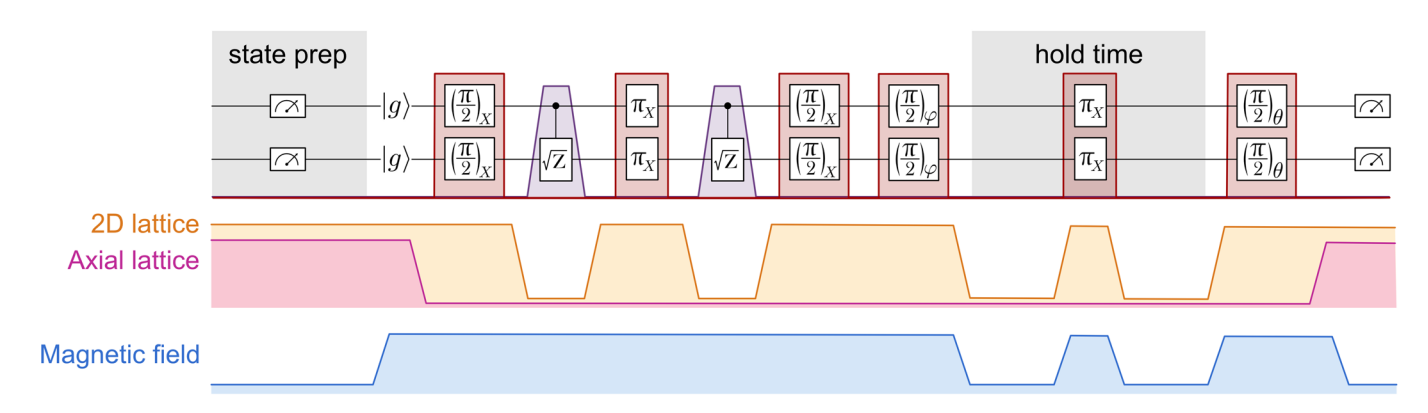


Extended Data Fig. 1 | FIG. M1. Trapping potentials of our apparatus. Our experiments make use of three separate optical trapping potentials. After producing a cold atomic sample via standard MOT techniques, we load atoms into an array of 515 nm optical tweezers projected through a high-numerical-aperture objective. This forms a 2d array of atoms which are then transfered into a single plane of a 3d optical lattice which is formed by two separate optical systems. First, a 2d bowtie lattice is formed using a single beam redirected by a series of mirrors and lenses. A second, axial lattice is projected from the side by directing two path-length-matched beams into a single aspheric lens.

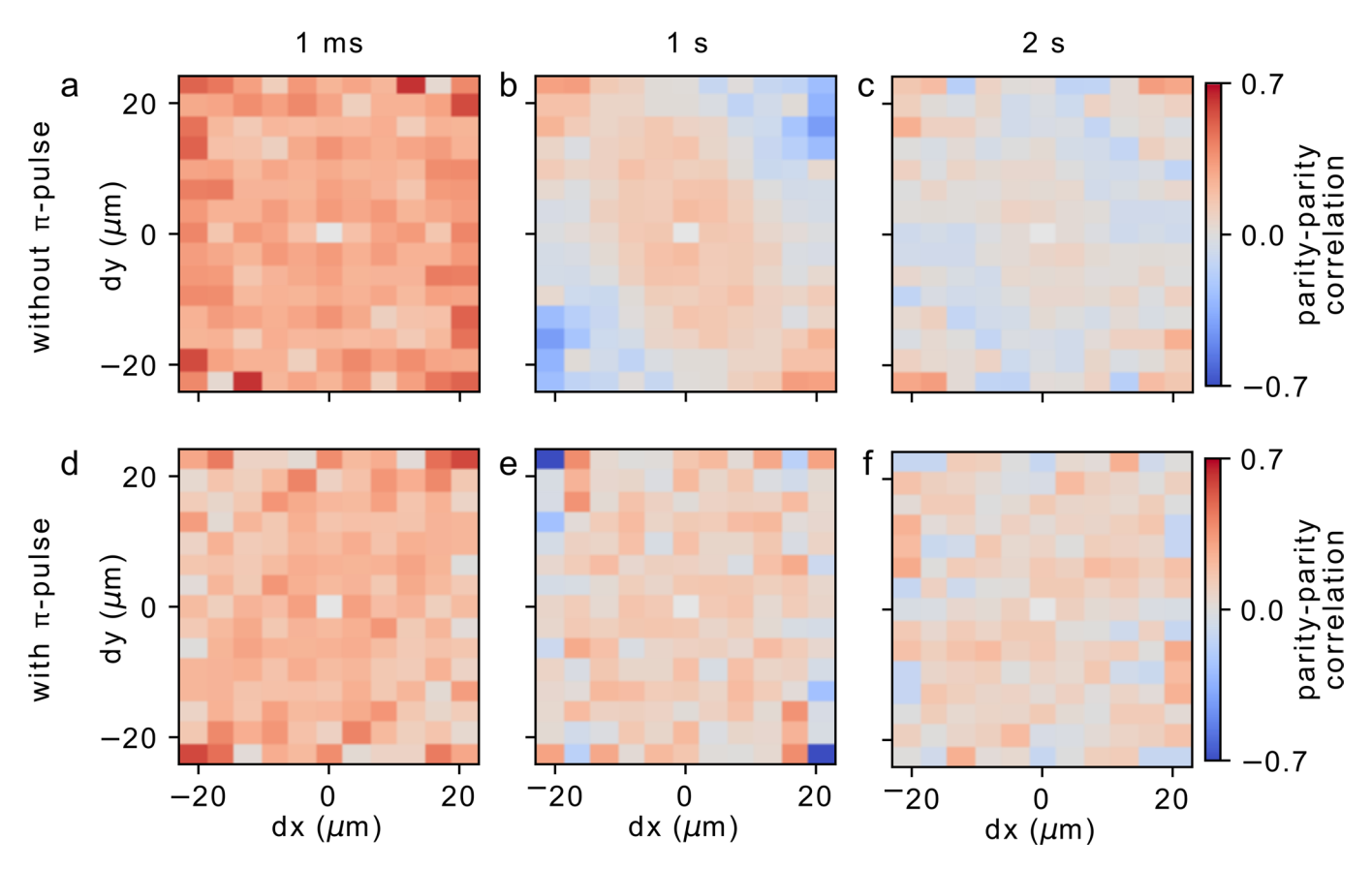




Extended Data Fig. 2 | FIG. M2. Single atom control. a) Tight atomic confinement and a 550 G magnetic field enable a clock Rabi frequency above 1 kHz with π -pulse fidelity well above 99%; however, fidelity is limited to 99.41(57)% in part by atomic heating (which also causes dephasing at later times, see SI). **Inset** shows the corresponding clock transition π -pulse spectrum. **b)** A UV laser near 317 nm drives a clock-Rydberg transition with Rabi with frequency $\Omega_r = 2\pi \times 13$ MHz. We detect the Rydberg state via loss of the clock state atoms. The horizontal dashed line represents an 89% Rydberg detection fidelity estimated from branching ratios of intermediate triplet *S* states (see text).



Extended Data Fig. 3 | FIG. M3. Experimental Sequence. We present a more detailed view of the experimental sequence that includes the clock laser pulses (red), the Rydberg laser pulses (purple), the 2d lattice (orange), the axial lattice (pink), and the z-component of the magnetic field (blue). Typical lattice ramping times are 3-10 ms, and we allow the magnetic field to ramp and settle for 100 ms. Although we can achieve clock Rabi frequencies as high as 1 kHz, we operate a factor of 10 slower to reduce the effect of magnetic field noise. As such, the total gate time from the first $\pi/2$ -pulse through the second $\pi/2$ -pulse is 22.2 ms, with 12 ms arising from the four 2d lattice ramps within the gate sequence.



Extended Data Fig. 4 | FIG. M4. Removing inhomogeneous lightshifts across the atom array. The lattice potential that confines the atoms during hold times is not perfectly magic or homogeneous, which can limit array-averaged correlation signals. By increasing lattice laser detuning from the magic condition, we more clearly reveal the effects of a non-magic-lattice inhomogeneity in spatially resolved parity-parity correlation measurements at short times (**a,d**), after 1 second (**b,e**), and after 2 seconds (**c,f**). The location of each pixel corresponds to a displacement vector between fully filled doublets, while the color corresponds to the product of the parities of each doublet with that displacement vector. **a-c)** Even in a shallow lattice condition, significant residual inhomogeneous lightshifts result in negative parity-parity correlations appearing along the main diagonal, reducing the array-averaged parity-parity correlator. **d-f**) Introducing a π-pulse half way through the hold time spin-echoes away the inhomogeneity, increasing the array-averaged parity-parity correlator.

Parameter	Figure 2d	Figure 3a,b	Figure 4a-e	Figure 4a	4f,g
			blue, gray	purple	
Rydberg detuning (initial, final) $(2\pi \times MHz)$	(40,2)	(22,2)	(22,5.8)	(40,4)	(40,8)
UV ramp time (ns)	350	250	250	350	350
Rydberg Rabi frequency $(2\pi \times MHz)$	14	16	16	10	16
Resonant gate time (ns)	varied	21	20	250	115
Lattice states during UV pulses (2d, axial) (E_r)	(0,0)	(12,8)	(12,8)	(0,0)	(0,0)
Magnetic field (during hold time if applicable) (G)	550	55	55 (2.8)	55 (55)	55

Extended Data Table 1 | TABLE M1. Experimental Parameters. Select parameters are tabulated for each dataset presented in the main text.